

**SnTe-AgBiTe₂ as efficient thermoelectrics with low thermal conductivity**

Journal:	<i>Journal of Materials Chemistry A</i>
Manuscript ID:	TA-ART-10-2014-005530
Article Type:	Paper
Date Submitted by the Author:	16-Oct-2014
Complete List of Authors:	Tan, Gangjian; Northwestern University, Department of Chemistry Shi, Fengyuan; Northwestern University, Department of Materials Science and Engineering Sun, Hui; University of Michigan, Department of Physics Zhao, Li-Dong; Northwestern University, Department of Chemistry Uher, Ctirad; University of Michigan, Department of Physics Dravid, Vinayak; Northwestern University, Department of Materials Science and Engineering; Northwestern University, Kanatzidis, Mercouri; Northwestern University, Department of Chemistry

SCHOLARONE™
Manuscripts

SnTe-AgBiTe₂ as efficient thermoelectrics with low thermal conductivity

Gangjian Tan,¹ Fengyuan Shi,² Hui Sun,³ Li-Dong Zhao,¹ Ctirad Uher,³ Vinayak P. Dravid,² and Mercouri G. Kanatzidis^{1,4,*}

¹Department of Chemistry, Northwestern University, Evanston, Illinois 60208, United States

²Department of Materials Science and Engineering, Northwestern University, Evanston, Illinois 60208, United States

³Department of Physics, University of Michigan, Ann Arbor, Michigan 48109, United States

⁴Materials Science Division, Argonne National Laboratory, Argonne, Illinois 60439, United States

*Corresponding author: m-kanatzidis@northwestern.edu

Abstract

SnTe is an intriguing alternative to its sister compound PbTe in thermoelectric energy conversion because of their electronic and structural similarity; however, it is challenging to optimize its thermoelectric performance to the level of PbTe because of the difficulties in decreasing its intrinsically large hole population and high thermal conductivity arising from the tin vacancies. We demonstrate here that by alloying some AgBiTe₂ in SnTe, thus forming AgSn_xBiTe_{x+2} compositions the hole concentration can be duly decreased because of the high efficiency of Bi as an electron donor. The lattice thermal conductivity is also decreased due to the strong scattering of phonons (by point defect scattering as well as Ag-rich nanostructures) to achieve a value of $\sim 0.7 \text{ W m}^{-1}\text{K}^{-1}$ at $\sim 750 \text{ K}$. As a result, a high thermoelectric figure *ZT* of merit of ~ 1.1 at 775 K is achieved by chemical composition optimization, making lead free SnTe-AgBiTe₂ promising thermoelectric materials.

Keywords: lead free; SnTe; thermoelectric; nanostructuring

1. Introduction

Lead chalcogenides and their solid solutions have been extensively investigated during the past several decades as robust thermoelectric materials with the highest figure of merit ZT exceeding 2.0 and have been proven to be very thermally stable.¹⁻⁷ The perceived toxicity of lead chalcogenides has raised interest in exploring Pb-free alternatives such as the isostructural SnTe for thermoelectric power generation.⁸⁻¹²

SnTe is well-known as a non-stoichiometric p-type semiconductor with a very high hole concentration of 10^{20} - 10^{21} cm⁻³ at room temperature arising from the intrinsically present Sn vacancies.^{13, 14} These inevitably lead to a very low Seebeck coefficient and a high electronic contribution to the total thermal conductivity in SnTe. Conventional doping cannot significantly decrease the hole population of SnTe,^{12, 15} although we recently reported a relatively low hole concentration of $\sim 5 \times 10^{19}$ cm⁻³ in Sn self-compensated SnTe via Cd doping.¹¹

It was previously reported that by alloying a proper amount of AgSbTe₂ with SnTe, creating the quaternary system AgSn_mSbTe_{m+2}, the hole concentration of SnTe can be reduced (not by Hall measurement) as evidenced by the variation of the Seebeck coefficient as a function of m.⁸ The most recent study of this system by Xing et al., however, pointed towards an opposite direction that the hole concentration of SnTe increases with increasing AgSbTe₂ although curiously the Seebeck coefficient also increased in this process.¹⁶ These results suggest that the introduction of AgSbTe₂ warrants additional investigations regarding its role in affecting the hole population of SnTe. Despite this, the presence of AgSbTe₂ in SnTe can greatly decrease the lattice

thermal conductivity of SnTe by the nanostructuring scattering of phonons^{8, 17, 18} ($\text{AgSn}_m\text{SbTe}_{m+2}$ system (TAST) is a nanostructured composite^{17, 18}) similar to the $\text{AgPb}_m\text{SbTe}_{m+2}$ systems (LAST)¹.

As a dopant bismuth has a contrasting role in lead chalcogenides^{4, 19} with respect to antimony although they are very chemically similar, lying in the fact that Bi is a more efficient electron donor while Sb is more helpful to create nanostructures. This motivates us to investigate what would happen if Sb is totally replaced by Bi in $\text{AgSn}_m\text{SbTe}_{m+2}$. We demonstrate here that the SnTe-AgBiTe₂ system with general chemical composition of $\text{AgSn}_x\text{BiTe}_{x+2}$ has much higher Seebeck coefficients than those of $\text{AgSn}_m\text{SbTe}_{m+2}$. This affirms that Bi is more powerful in neutralizing the holes in SnTe than Sb, with the highest value approaching $\sim 180 \mu\text{V/K}$ around 800 K by tuning x. Interestingly, we also observe dispersed nanoscale precipitates that are evenly and coherently distributed within the SnTe matrix, which suggests that the SnTe-AgBiTe₂ system is not only a solid solution. These distinctive nanostructures coupled with the point defect scattering by Ag and Bi alloying at Sn sites give rise to a very low lattice thermal conductivity of $\sim 0.7 \text{ W/mK}$ at $\sim 750 \text{ K}$ in $\text{AgSn}_x\text{BiTe}_{x+2}$. Consequently, an optimized ZT of ~ 1.1 is achieved around 800 K for the nominal composition of $x=15$, which makes the SnTe-AgBiTe₂ system attractive in mid-temperature thermoelectric power generation.

2. Experimental section

Synthesis

Reagent chemicals were used as obtained: Ag chunk (99.99%, American

Elements, US), Sn chunk (99.999%, American Elements, US), Bi shot (99.999%, American Elements, US), and Te shot (99.999%, 5N Plus, American Elements).

Synthesis of Starting Materials: Samples with nominal compositions SnTe and $\text{AgSn}_x\text{BiTe}_{x+2}$ ($x=25, 20, 15, 10, \text{ and } 5$) were prepared as follows. Appropriate amounts of Ag, Sn, Bi, and Te were weighed and mixed in 10 mm diameter silica tubes. The tubes were then evacuated to a residual pressure of $\sim 10^{-4}$ Torr, flame-sealed, slowly heated to 1273 K in 10 h, soaked at this temperature for 6 h, then slowly cooled down to 1073 K in 2 h, dwelled at this temperature for 4 h, and then slowly cooled to room temperature by switching off the furnace power. To help improve the homogeneity of the samples, the tubes were periodically shaken in the melting process. For a typical experiment: Ag (0.2023 g, 1.8751 mmol), Sn (3.3384 g, 28.1268 mmol), Bi (0.3919 g, 1.8751 mmol), and Te (4.0675 g, 31.8770 mmol) were used to prepare 8 g of $\text{AgSn}_{15}\text{BiTe}_{17}$ sample.

The melt grown ingots were ground into fine powders using a mechanical mortar and pestle to reduce the grains to less than 4 μm in diameter. These powders were then densified by spark plasma sintering (SPS) method (SPS-211LX, Fuji Electronic Industrial Co., Ltd.) at 723 K for 5 min in a 12.7 mm diameter graphite die under an axial pressure of 40 MPa in vacuum. Highly dense (>97% of theoretical density, Table S1) disk-shaped pellets with dimensions of 12.7 mm diameter and 8 mm thickness were obtained. Bars and squares were cut from the same sample pellets for high temperature thermoelectric property measurements.

Physical Characterization

Electrical Properties: The SPSed pellets were cut into 12 mm × 3 mm × 3 mm bars for simultaneous measurement of the Seebeck coefficient and the electrical conductivity using an Ulvac Riko ZEM-3 instrument under a low-pressure helium atmosphere from room temperature to 800 K. The uncertainty of the Seebeck coefficient and electrical conductivity measurements is 5%.

Thermal Conductivity: The SPSed pellets were cut and polished into a squared shape of 6×6×2 mm³ for thermal diffusivity measurements. The thermal diffusivity coefficient (D) was measured using the laser flash diffusivity method in a Netzsch LFA457, the specific heat capacity (C_p) was indirectly derived using a representative sample (Pyroceram 9606) in the range 300-800 K, and the density (d) was determined using the dimensions and mass of the sample. The thermal conductivity was calculated from $\kappa = D \cdot C_p \cdot d$. The uncertainty of the thermal conductivity is estimated to be within 8%, considering the uncertainties from D , C_p , and d . The thermal diffusion and the heat capacity data for all samples can be found in the Supporting Information (Figure S1). The combined uncertainty for all measurements involved in the calculation of ZT is less than 15%.

Hall Measurements: The room temperature Hall measurement was performed on a homemade apparatus (University of Michigan). The Hall resistance was monitored with a Linear Research AC Resistance Bridge (LR-700), with constant magnetic fields of ±1 T applied by using an Oxford Superconducting magnet.

Electron Microscopy and X-ray Diffraction

(Scanning) transmission electron microscopy ((S)TEM), STEM electron energy

loss spectroscopy (EELS) and STEM energy dispersive spectroscopy (EDS) investigations were carried out using a JEOL 2100F microscope operated at 200 kV. Thin TEM specimens were prepared by conventional methods, including cutting, grinding, dimpling, tripod, with minimal duration of Ar-ion milling, and followed by liquid nitrogen cooling, low energy (900 eV) ion milling by Fischione Nanomill. Samples pulverized with an agate mortar were used for powder X-ray diffraction (XRD). The powder diffraction patterns were obtained with Cu K α ($\lambda = 1.5418 \text{ \AA}$) radiation in a reflection geometry on an Inel diffractometer operating at 40 kV and 20 mA and equipped with a position-sensitive detector.

3. Results and discussion

Phase composition

Figure 1(a) shows the powder XRD patterns for SnTe and AgSn_xBiTe_{x+2} after SPS processing in this study. All Bragg diffraction peaks can be indexed in the cubic NaCl-type structure, space group *Fm-3m*, and no obvious second phase can be detected. The lattice parameters decrease with increasing AgBiTe₂ content, which is consistent with the difference of lattice parameter between NaCl-structured SnTe (6.3093 Å)²⁰ and AgBiTe₂ (6.155 Å)²¹, Figure 1(b). However, it should be noted that the variation of the lattice parameter for AgSn_xBiTe_{x+2} does not strictly follow the Vegard's law indicated by the solid line, Figure 1(b). This suggests that SnTe-AgBiTe₂ system cannot be simply viewed as a solid solution. Indeed, as will be shown later (Figure 5), a considerable amount of nanoscaled precipitates is found in AgSn_xBiTe_{x+2}.

under TEM observation (see below), which is quite similar to the SnTe-AgSbTe₂ and LAST systems^{1, 17, 18}.

Figures 2(a) displays the room temperature hole concentration as a function of AgBiTe₂ fraction in AgSn_xBiTe_{x+2}. For typical semiconductors, if iso-electronically substituted, the carrier density will remain unchanged. However, we find that the hole density of the samples is decreased even when a small amount of AgBiTe₂ ($x=25$) is involved, while when more AgBiTe₂ participates ($x<25$), the hole concentration increases gradually. We conjecture that at a small level of AgBiTe₂, Ag and Bi mainly occupy Sn lattices. Unlike SnTe, AgBiTe₂ is stoichiometric.²² Thus the incorporation of AgBiTe₂ in SnTe can effectively compensate the Sn vacancies and decrease the hole population. However, when more AgBiTe₂ is added, the AgSn_xBiTe_{x+2} compositions tend to be phase segregated (on the nanoscale as we show below) rather than form a complete solid solution. The phase segregation is associated with formation of nanostructures which change the chemical composition of the matrix and thus the hole density. On the other hand, when more AgBiTe₂ is involved, the band gap of SnTe becomes smaller (see discussion below), which would probably decrease the defect formation energy and increase the Sn vacancies, contributing to increased hole densities. A comparison of the hole concentrations of AgSn_xBiTe_{x+2} and AgSn_mSbTe_{m+2},¹⁶ Figure 2(a), clearly shows that the former has much lower hole concentrations than the latter under the same x or m. This indicates that Bi is a more effective electron donor than Sb in SnTe and is consistent with previous findings in other II-VI systems.^{4, 19} The carrier mobility decreases monotonically with increasing

AgBiTe₂ content, Figure 2(b), suggesting an enhanced point defect and interfacial scattering by nanostructures (described below).

Electrical properties

The temperature dependent electrical conductivities for AgSn_xBiTe_{x+2} are shown in Figure 3(a). For all samples, the electrical conductivity steadily decreases with increasing temperature (typical of metallic behavior) except for the sample with x=5 which clearly shows turnover behavior around 600 K (inset of Figure 3(a)) despite the fact that it has the highest hole density at room temperature (Figure 2(a)). With increasing AgBiTe₂ content the room temperature electrical conductivity decreases gradually from ~7800 S/cm for SnTe to ~1000 S/cm for x=5 sample, which is mainly ascribed to the loss of carrier mobility, Figure 2(b).

The Seebeck coefficients as a function of temperature for AgSn_xBiTe_{x+2} are shown in Figure 3(b). They clearly indicate an increasing trend at room temperature with increasing AgBiTe₂ content although the hole concentrations also increase (SnTe excluded). This abnormal dependence of the hole concentration is related to the two-valence band nature of the electronic structure of SnTe.^{11, 12, 23, 24}

The band gap E_g of typical semiconductors can be assessed using the Goldsmid relation: $E_g = 2eS_{\max}T_{\max}$,²⁵ where e is the electron charge and T_{\max} is the temperature at which the maximum Seebeck coefficient S_{\max} occurs. Applying this relation to resolve E_g for samples with lower AgBiTe₂ content is unsuccessful in this case because no sign of turnover is reflected in the $S-T$ plot. However, we can estimate the band gaps of x=10 and x=5 samples (they clearly show turnover of Seebeck coefficient) to be

~0.22 and ~0.14 eV, respectively. This decreasing trend in band gap of $\text{AgSn}_x\text{BiTe}_{x+2}$ with increasing AgBiTe_2 content can reasonably explain why the $x=5$ sample shows a turnover in $\sigma-T$ plot at a very low temperature despite its highest hole concentration, and is consistent with the very low band gap of AgBiTe_2 (~0.16 eV) which is in fact smaller than that of SnTe (~0.19 eV) at room temperature²⁶ (we note that the band gap of SnTe is temperature dependent, so at elevated temperature the band gap of SnTe should be larger than 0.19 eV. This can account for the estimated band gap of the $x=10$ sample being slightly larger than the end compositions).

The composition dependent Seebeck coefficients for SnTe-AgBiTe_2 and SnTe-AgSbTe_2 systems at room temperature and at 700 K are plotted in Figure 3(c). Clearly, with identical AgBiTe_2 and AgSbTe_2 content, $\text{AgSn}_x\text{BiTe}_{x+2}$ have much higher Seebeck coefficients because Bi is more effective than Sb in neutralizing holes of SnTe as mentioned above,^{4, 19} Figure 2(a).

Figure 3(d) shows the temperature dependent power factors for $\text{AgSn}_x\text{BiTe}_{x+2}$ samples. For the samples with less AgBiTe_2 content (SnTe , $x=25$, 20, and 15), the power factors increase steadily with rising temperature. The $x=10$ and 5 samples have higher power factors near room temperature but much lower at elevated temperatures due to bipolar conduction. The maximum power factor reaches ~23 $\mu\text{Wcm}^{-1}\text{K}^{-2}$ around 750 K for the $\text{AgSn}_{15}\text{BiTe}_{17}$ sample, which is comparable to that of the optimized $\text{AgSn}_m\text{SbTe}_{m+2}$ system.^{8, 16} However, lower electrical conductivities in $\text{AgSn}_x\text{BiTe}_{x+2}$ than in $\text{AgSn}_m\text{SbTe}_{m+2}$ suggest smaller electronic contributions to the respective total thermal conductivities.

Thermal conductivity

The temperature dependent total thermal conductivities (κ_{tot}) for $\text{AgSn}_x\text{BiTe}_{x+2}$ are shown in Figure 4(a). For SnTe itself κ_{tot} is very high at $\sim 8 \text{ Wm}^{-1}\text{K}^{-1}$ at 300 K and decreases steadily with increasing temperature, approaching $\sim 3.3 \text{ Wm}^{-1}\text{K}^{-1}$ at 800 K. It is evident that the introduction of AgBiTe_2 , even in a very small amount, can efficiently decrease κ_{tot} of SnTe. For example, κ_{tot} for $\text{AgSn}_{25}\text{BiTe}_{27}$ are only ~ 3.4 and $\sim 2.2 \text{ Wm}^{-1}\text{K}^{-1}$ at 300 and 800 K respectively. Moreover, further reduction in κ_{tot} is obtained when more AgBiTe_2 is introduced. The lowest κ_{tot} at room temperature is $\sim 1.6 \text{ Wm}^{-1}\text{K}^{-1}$ achieved in $\text{AgSn}_5\text{BiTe}_7$, which is quite close to that of Bi_2Te_3 -based materials.²⁷ In the samples with high AgBiTe_2 ($x=10$ and 5), however, serious bipolar diffusion phenomena are observed due to band gap narrowing, giving rise to a very high κ_{tot} at high temperature.

The lattice thermal conductivity κ_{lat} can be obtained by removing the electronic contribution κ_{ec} from κ_{tot} according to the Wiedemann-Franz relation $\kappa_{\text{ec}}=L\sigma T$. The Lorenz number L is calculated by fitting the Seebeck coefficient data to the reduced chemical potential using a single parabolic band model with acoustic phonon scattering,²⁸ Figure S1. Figure 4(b) shows the lattice thermal conductivity (κ_{lat}) as a function of temperature for $\text{AgSn}_x\text{BiTe}_{x+2}$. Clearly, SnTe has the highest κ_{lat} among all samples over the entire temperature range. With increasing AgBiTe_2 content, κ_{lat} decreases gradually and bipolar diffusion becomes evident. A rather low κ_{lat} of $\sim 0.7 \text{ Wm}^{-1}\text{K}^{-1}$ at $\sim 750 \text{ K}$ is seen in the $x=15$ sample, which is very close to the value found in Cd-doped SnTe nanostructuring with CdS¹¹ and also approaches the theoretically

minimum thermal conductivity κ_{\min} of $\sim 0.5 \text{ W m}^{-1}\text{K}^{-1}$ for SnTe based materials calculated using the model proposed by Cahill et al.²⁹:

$$\kappa_{\min} = \frac{\pi}{4} k_B V^{-\frac{2}{3}} v \quad (1)$$

where V is the unit cell volume, k_B the Boltzmann constant, and v the sound velocity ($\sim 1800 \text{ m/s}$ for SnTe³⁰).

To examine the origin of low κ_{lat} in the $\text{AgSn}_x\text{BiTe}_{x+2}$ system, the Klemens-Drabble (KD) theory³¹ of disordered alloys was adopted to analyze the contribution of point defect scattering (pure alloying effect of AgBiTe_2 with SnTe) to the reduction of κ_{lat} of SnTe based materials. In KD theory, the lattice thermal conductivity of a disordered alloy κ_{lat}^d is determined by³¹⁻³³:

$$\kappa_{\text{lat}}^d = \frac{\tan^{-1}(u)}{u} \kappa_{\text{lat}}^p \quad (2)$$

where κ_{lat}^p is the lattice thermal conductivity of a pure alloy and u can be expressed by:

$$u^2 = \frac{\pi^2 \Theta_D \Omega}{h v^2} \kappa_{\text{latt}}^p \Gamma \quad (3)$$

here Θ_D is the Debye temperature, Ω the molar volume, h the Plank constant, v the sound velocity, and Γ the disorder scaling parameter depending on mass and strain field fluctuations. For a pseudo-binary ((AC)_{1-x}(BC)_x type) system:

$$\Gamma = x(1-x) \left[\left(\frac{\Delta M}{M} \right)^2 + \varepsilon \left(\frac{\Delta a}{a} \right)^2 \right] \quad (4)$$

where ε is a phenomenological parameter related to the Grüneisen parameter γ , M and a are the molar mass and lattice constant of the alloy, ΔM and Δa are the difference in mass and lattice constant between the two constituents. We then used the reference

values of $\Theta_D=140$ K,³⁴ $v=1800$ m/s,³⁰ and $\epsilon=65$ ³⁵ for the calculation of lattice thermal conductivities as a function of AgBiTe₂ fraction for AgSn_xBiTe_{x+2}, see the solid line in Figure 4(c). It is clear that KD prediction line lies well above the experimental data points, especially for those with higher AgBiTe₂ content. This suggests that additional phonon scattering factors are at play in these materials. We show later that the endotaxial Ag-rich nanoscale precipitates homogeneously embedded within SnTe matrix may serve as additional strong phonon scattering agents.

The ZT values as a function of temperature for AgSn_xBiTe_{x+2} are shown in Figure 4(d). The samples show monotonically increasing ZT with rising AgBiTe₂ content around room temperature, however, occurrence of bipolar conduction seen in the samples with high AgBiTe₂ content ($x=10$ and 5) leads to serious deterioration of ZT at high temperatures for these systems. A maximum ZT of ~ 1.1 is achieved around 775 K for AgSn₁₅BiTe₁₇, which is $\sim 140\%$ improvement over the pristine SnTe. This value is also higher than the best result (~ 1.0) achieved in AgSn_mSbTe_{m+2}⁸ and arises from the larger Seebeck coefficients of the SnTe-AgBiTe₂ system.

All-scale hierarchical microstructures

The microstructure, crystallography, grain structure and composition analysis of the specimens were investigated using high-resolution TEM (HRTEM), STEM electron energy loss spectroscopy (EELS) and STEM energy dispersive spectroscopy (EDS).

Meso-scale microstructures shown in Figure 5(a) are created by the powder processing and SPS treatment. Figure 5(b) shows nanoscale precipitates with darker

contrast in the medium magnification TEM image taken along $B = [001]$. The upper left inset HRTEM image depicts a nanoscale precipitate with coherent interfaces with the matrix, highlighted by the dashed white circle. The lower left inset shows a selected area electron diffraction (SAED) pattern along [001] orientation with an aperture capturing both the matrix and the nanoscale precipitates, which shows only one set of Bragg diffraction points, suggesting no distinguishable difference between the matrix and the nanoscale precipitate lattice spacings, owing to their small lattice mismatch and endotaxial relationship.

STEM EELS and EDS were also applied to study the compositions of the nanoscale precipitates as shown in the supplementary results (Figure S2). STEM EELS spectrum imaging (SI) reveals that the nanoscale precipitates are rich in Ag but deficient in Sn and Te, which is very similar to the observations in LAST system^{1,36-39}. STEM EDS results also suggest that Ag and Bi are alloyed in the matrix (Figure S2(e)), which may create additional point defects for scattering phonons. We have also employed statistical analysis to obtain the grain size distribution (Figure 5(c)) and the precipitates size distribution (Figure 5(d)) of the specimen along [001] orientation with the representative areas shown in Figure 5(a) and (b), respectively. The grain size is estimated ranging from 300 nm to 1.6 μm and the precipitate size is ranging from 3 nm to 9 nm. The all-scale hierarchical structures are proven to be effective to scatter phonons with different mean free paths,^{7, 40} which decreases the lattice thermal conductivity as shown in Figure 4(b) and improves the ZT values of SnTe as shown in Figure 4(d).

4. Concluding remarks

The introduction of AgBiTe₂ in SnTe can yield high thermoelectric performance. Compared to the SnTe-AgSbTe₂ system, much higher Seebeck coefficients can be achieved in SnTe-AgBiTe₂ because Bi is more efficient than Sb in neutralizing holes. We also uncovered that similar to SnTe-AgSbTe₂, SnTe-AgBiTe₂ system is more than a solid solution. As evidenced by TEM observations, dense nanoprecipitates with Ag-rich composition are homogeneously distributed within the matrix, together with significant point defect scattering by AgBiTe₂ alloying, giving rise to a sufficiently low lattice thermal conductivity in AgSn_xBiTe_{x+2} system. Consequently, a high *ZT* value of ~1.1 is achieved at 775 K for the sample with x=15, which makes lead free SnTe-AgSbTe₂ as promising materials for thermoelectric power generation.

Acknowledgements

This work was supported as part of the Revolutionary Materials for Solid State Energy Conversion, an Energy Frontier Research Center funded by the U.S. Department of Energy, Office of Science, and Office of Basic Energy Sciences under Award Number DE-SC0001054. Transmission electron microscopy work was partially performed in the EPIC facility of the NUANCE Center at Northwestern University.

References

1. K. F. Hsu, S. Loo, F. Guo, W. Chen, J. S. Dyck, C. Uher, T. Hogan, E. Polychroniadis and M. G. Kanatzidis, *Science*, 2004, **303**, 818-821.
2. J. P. Heremans, V. Jovovic, E. S. Toberer, A. Saramat, K. Kurosaki, A. Charoenphakdee, S. Yamanaka and G. J. Snyder, *Science*, 2008, **321**, 554-557.

3. Y. Pei, X. Shi, A. LaLonde, H. Wang, L. Chen and G. J. Snyder, *Nature*, 2011, **473**, 66-69.
4. Y. Lee, S.-H. Lo, C. Chen, H. Sun, D.-Y. Chung, T. C. Chasapis, C. Uher, V. P. Dravid and M. G. Kanatzidis, *Nat. Commun.*, 2014, **5**.
5. H. Wang, Y. Pei, A. D. LaLonde and G. J. Snyder, *Adv. Mater.*, 2011, **23**, 1366-1370.
6. L.-D. Zhao, J. He, S. Hao, C.-I. Wu, T. P. Hogan, C. Wolverton, V. P. Dravid and M. G. Kanatzidis, *J. Am. Chem. Soc.*, 2012, **134**, 16327-16336.
7. L. Zhao, H. Wu, S. Hao, C. Wu, X. Zhou, K. Biswas, J. He, T. Hogan, C. Uher and C. Wolverton, *Energy Environ. Sci.*, 2013, **6**, 3346-3355.
8. M. K. Han, J. Androulakis, S. J. Kim and M. G. Kanatzidis, *Adv. Energy Mater.*, 2012, **2**, 157-161.
9. Y. Chen, M. D. Nielsen, Y. B. Gao, T. J. Zhu, X. Zhao and J. P. Heremans, *Adv. Energy Mater.*, 2012, **2**, 58-62.
10. A. Banik and K. Biswas, *J. Mater. Chem. A*, 2014, **2**, 9620-9625.
11. G. Tan, L.-D. Zhao, F. Shi, J. W. Doak, S.-H. Lo, H. Sun, C. Wolverton, V. P. Dravid, C. Uher and M. G. Kanatzidis, *J. Am. Chem. Soc.*, 2014, **136**, 7006-7017.
12. Q. Zhang, B. Liao, Y. Lan, K. Lukas, W. Liu, K. Esfarjani, C. Opeil, D. Broido, G. Chen and Z. Ren, *P. Natl. Acad. Sci. USA*, 2013, **110**, 13261-13266.
13. R. Brebrick, *J. Phys. Chem. Solids*, 1963, **24**, 27-36.
14. V. Vedeneev, S. Krivoruchko and E. Sabo, *Semiconductors*, 1998, **32**, 241-244.
15. E. Rogacheva, *J. Phys. Chem. Solids*, 2008, **69**, 259-268.
16. Z.-B. Xing, Z.-Y. Li, Q. Tan, T.-R. Wei, C.-F. Wu and J.-F. Li, *J. Alloys. Compd.*, 2014, **615**, 451-455.
17. J. Androulakis, R. Pcionek, E. Quarez, J.-H. Do, H. Kong, O. Palchik, C. Uher, J. J. D'Angelo, J. Short and T. Hogan, *Chem. Mater.*, 2006, **18**, 4719-4721.
18. J. Androulakis, R. Pcionek, E. Quarez, O. Palchik, H. Kong, C. Uher, J. Dangelo, T. Hogan, X. Tang and T. Tritt, in *Mater. Res. Soc. Symp. Proc.*, Cambridge Univ Press, 2006, pp. 187-194.
19. M.-K. Han, K. Hoang, H. Kong, R. Pcionek, C. Uher, K. M. Paraskevopoulos, S. Mahanti and M. G. Kanatzidis, *Chem. Mater.*, 2008, **20**, 3512-3520.
20. N. Short, *J. Phys. D: Appl. Phys.*, 1968, **1**, 129-130.
21. J. Wernick, S. Geller and K. Benson, *J. Phys. Chem. Solids*, 1958, **7**, 240-248.
22. R. Sharma and Y. Chang, *Bulletin of Alloy Phase Diagrams*, 1986, **7**, 72-80.
23. R. Brebrick and A. Strauss, *Phys. Rev.*, 1963, **131**, 104-110.
24. L. Rogers, *J. Phys. D: Appl. Phys.*, 1968, **1**, 845-852.
25. H. Goldsmid and J. Sharp, *J. Electron. Mater.*, 1999, **28**, 869-872.
26. O. Madelung, *Semiconductors: data handbook*, Springer, 2004.
27. S. Wang, G. Tan, W. Xie, G. Zheng, H. Li, J. Yang and X. Tang, *J. Mater. Chem.*, 2012, **22**, 20943-20951.
28. D. M. Rowe, *CRC handbook of thermoelectrics*, CRC press, 1995.
29. D. G. Cahill, S. Watson and R. Pohl, *Phys. Rev. B*, 1992, **46**, 6131-6140.
30. P. Bauer Pereira, I. Sergueev, S. Gorsse, J. Dadda, E. Müller and R. P. Hermann, *Phys. Status Solidi B*, 2013, **250**, 1300-1307.

31. P. Klemens, *Phys. Rev.*, 1960, **119**, 507-509.
32. J. Yang, G. Meisner and L. Chen, *Appl. Phys. Lett.*, 2004, **85**, 1140-1142.
33. T. IRIE, *Jpn. J. Appl. Phys.*, 1966, **5**, 854-859.
34. S. Bukshpan, *Solid State Commun.*, 1968, **6**, 477-478.
35. G. Tan, F. Shi, J. W. Doak, H. Sun, L.-D. Zhao, P. Wang, C. Uher, C. Wolverton, V. P. Dravid and M. G. Kanatzidis, *Energy Environ. Sci.*, 2014.
36. B. A. Cook, M. J. Kramer, J. L. Harringa, M. K. Han, D. Y. Chung and M. G. Kanatzidis, *Adv. Funct. Mater.*, 2009, **19**, 1254-1259.
37. E. Levin, B. Cook, K. Ahn, M. Kanatzidis and K. Schmidt-Rohr, *Phys. Rev. B*, 2009, **80**, 115211.
38. J. Androulakis, K. F. Hsu, R. Pcionek, H. Kong, C. Uher, J. J. D'Angelo, A. Downey, T. Hogan and M. G. Kanatzidis, *Adv. Mater.*, 2006, **18**, 1170-1173.
39. E. Quarez, K.-F. Hsu, R. Pcionek, N. Frangis, E. Polychroniadis and M. G. Kanatzidis, *J. Am. Chem. Soc.*, 2005, **127**, 9177-9190.
40. K. Biswas, J. He, I. D. Blum, C.-I. Wu, T. P. Hogan, D. N. Seidman, V. P. Dravid and M. G. Kanatzidis, *Nature*, 2012, **489**, 414-418.

Electronic supplementary information (ESI) available: room temperature densities for all the samples investigated in this study (Table S1); thermal diffusivity, heat capacity, and Lorenz number for $\text{AgSn}_x\text{BiTe}_{x+2}$ samples (Figure S1); Compositional analysis by STEM EELS for $\text{AgSn}_{15}\text{BiTe}_{17}$ (Figure S2).

Figure captions

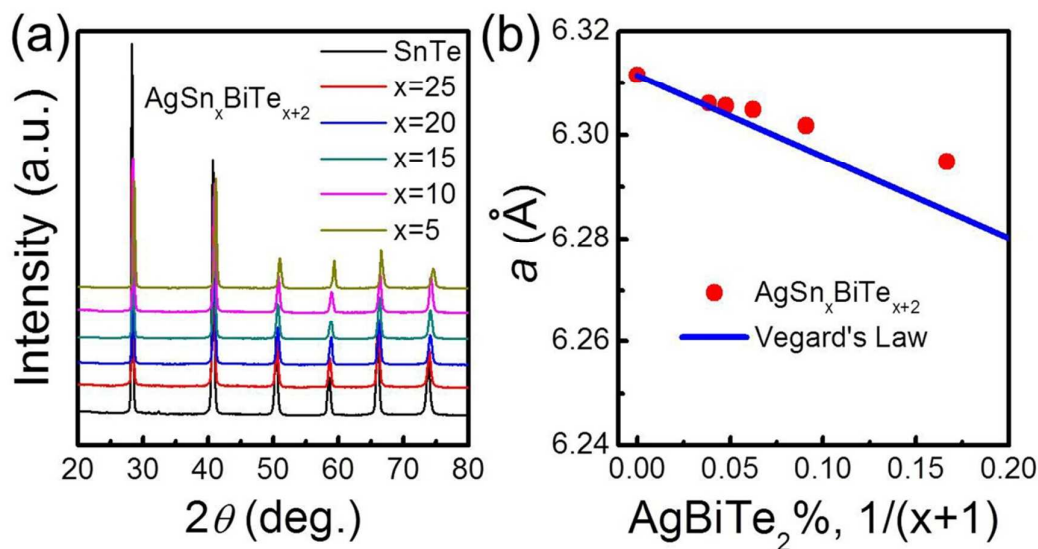
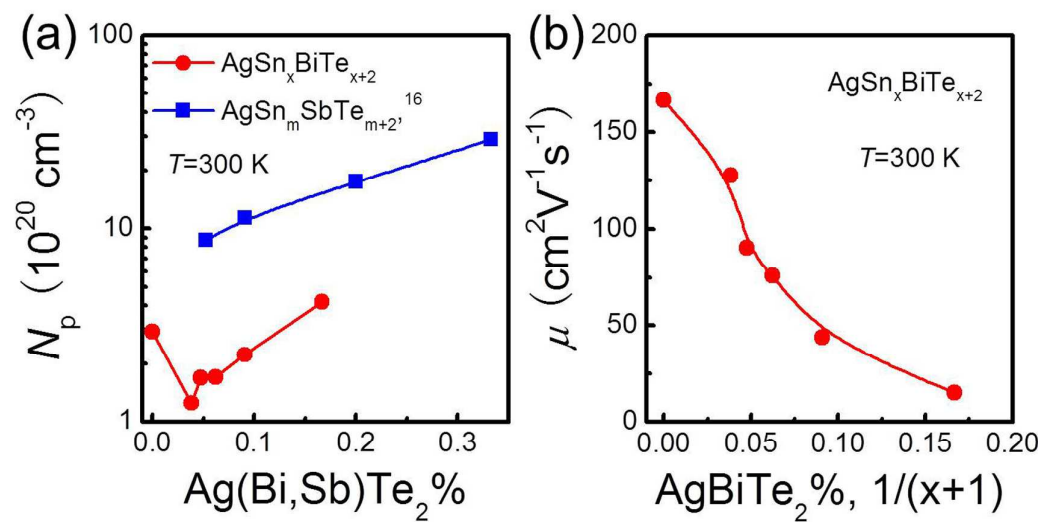
Figure 1. (a) Powder XRD patterns and (b) room temperature lattice parameters a for SnTe and $\text{AgSn}_x\text{BiTe}_{x+2}$ samples. Blue line in (b) is a theoretical prediction of lattice parameter according to Vegard's law.

Figure 2. Room temperature (a) Hall hole concentration N_p and (b) carrier mobility μ for SnTe and $\text{AgSn}_x\text{BiTe}_{x+2}$ samples. The hole densities of $\text{AgSn}_m\text{SbTe}_{m+2}$ system¹⁶ are also included in (a) for comparison.

Figure 3. (a) Electrical conductivities σ , (b) Seebeck coefficients S , and (d) power factors $S^2\sigma$ as a function of temperature for SnTe and $\text{AgSn}_x\text{BiTe}_{x+2}$ samples. Inset of (a) is an enlarged view of electrical conductivity for $x=5$ sample which shows a clear turnover around 600 K. (c) Seebeck coefficients for $\text{AgSn}_x\text{BiTe}_{x+2}$ (circles) and $\text{AgSn}_m\text{SbTe}_{m+2}$ (stars)^{8, 16} at 300 (in blue) and 800 K (in red), respectively. The lines are guide to eyes.

Figure 4. (a) Total thermal conductivities κ_{tot} , (b) lattice thermal conductivities κ_{latt} , and (d) ZT values as a function of temperature for SnTe and $\text{AgSn}_x\text{BiTe}_{x+2}$ samples. The solid line in (b) represents the theoretically minimum thermal conductivity for SnTe based materials. (c) room temperature lattice thermal conductivities as a function of AgBiTe₂ content for $\text{AgSn}_x\text{BiTe}_{x+2}$. 15 % error bars are indicated. The red line is a solid solution line predicted by the Klemens-Drabble (KD) model.

Figure 5. Electron microscopy of specimen $\text{AgSn}_{15}\text{BiTe}_{17}$. (a) A low-magnification image of meso-scale grains. False colors are used as guide to the eye. (b) Nanoscale precipitates with dark contrast are shown in the HRTEM image. The upper inset shows a HRTEM image of a nanoscale precipitate, highlighted by the dashed white circle. The lower inset is a selected area electron diffraction pattern with $B = [001]$. (c) and (d) are size distributions of meso-scale grains and nanoscale precipitates, respectively.

**Figure 1****Figure 2**

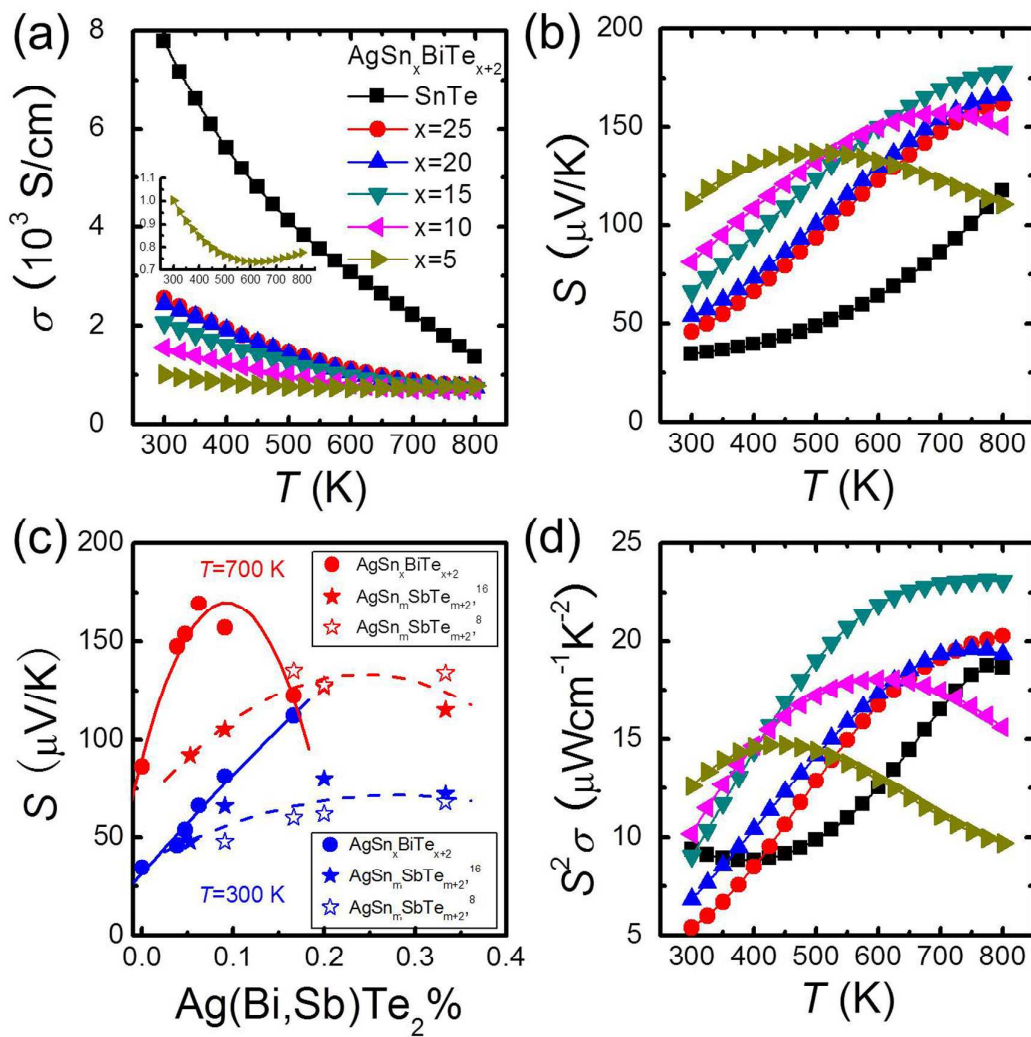


Figure 3

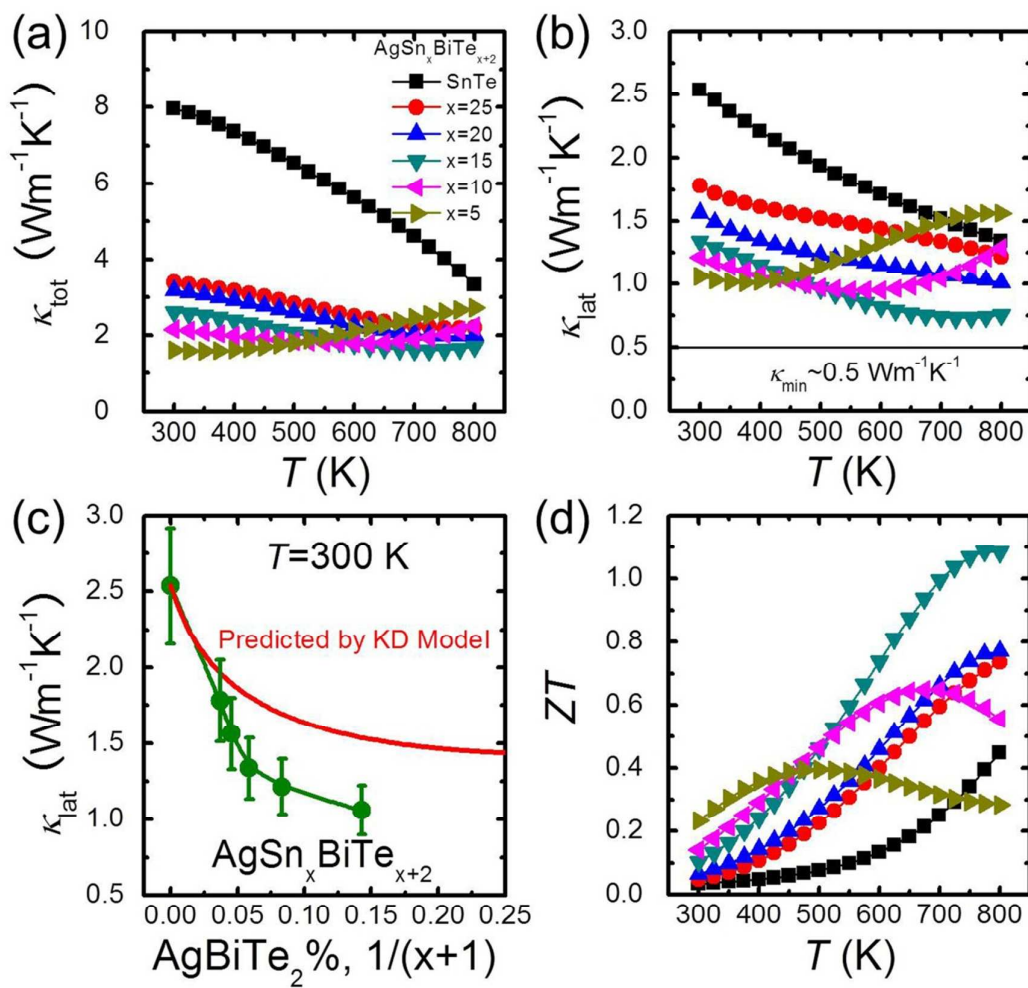


Figure 4

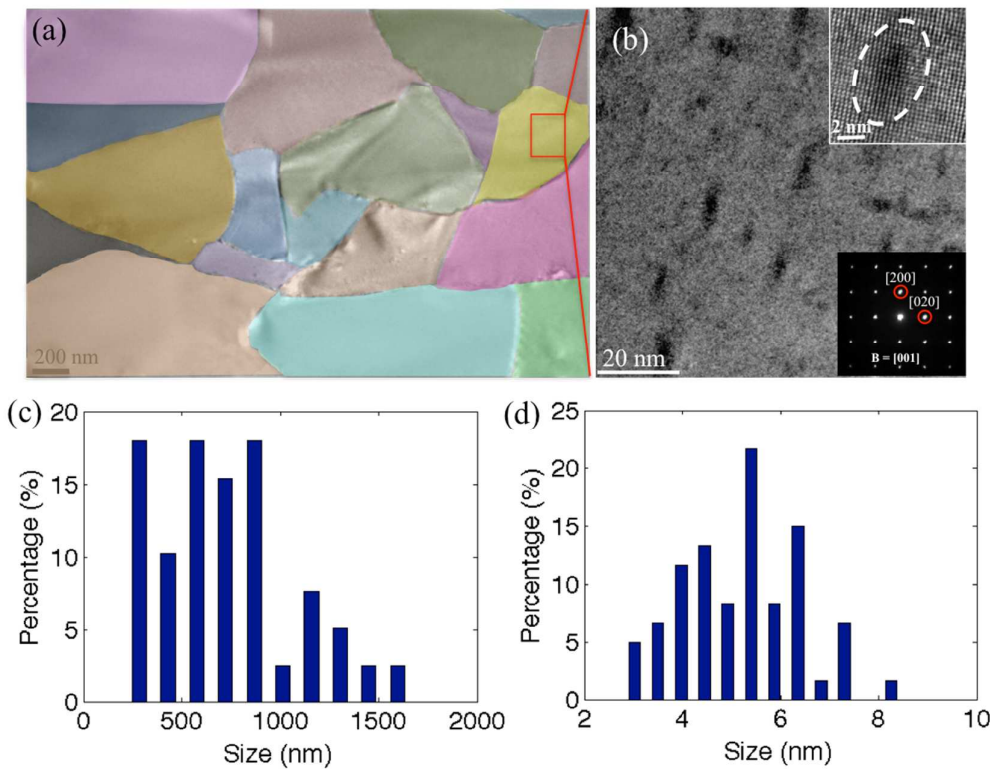


Figure 5